SCIENTIFIC REP⚙RTS

OPEN

Atomic-state diagnostics and optimization in cold-atom experiments

Krystian Sycz, Adam M. Wojciechowski (ID) & Wojciech Gawlik

We report on the creation, observation and optimization of superposition states of cold atoms. In our experiments, rubidium atoms are prepared in a magneto-optical trap and later, after switching off the trapping fields, Faraday rotation of a weak probe beam is used to characterize atomic states prepared by application of appropriate light pulses and external magnetic fields. We discuss the signatures of polarization and alignment of atomic spin states and identify main factors responsible for deterioration of the atomic number and their coherence and present means for their optimization, like relaxation in the dark with the strobed probing. These results may be used for controlled preparation of cold atom samples and *in situ* magnetometry of static and transient fields.

Precision spectroscopic measurements require adequate control of the quantum state of the atomic sample and of the environment in which atoms/molecules are contained. Representative examples include laser cooling and trapping of atoms[1], optical metrology with atom interferometry[2] and atomic clocks[3], and methods for changing speed of light propagating across atomic sample[4].

Many systems possess long-lived ground states with magnetic degeneracy, where the control is achieved by use of appropriate light, magnetic and radio-frequency (RF) fields to create and manipulate specific spin states[5–7]. Such states are conveniently described by polarization and/or alignment, i.e., appropriate elements of the system's density matrix[8,9].

Particular role in the experiments with superposition states is played by cold atoms which offer unique conditions, such as: (i) slowed-down all relaxation mechanisms, like atomic collisions (particularly the spin-exchange one), (ii) absence of velocity-averaging and related Doppler broadening, (iii) ability to address a single hfs transition, (iv) different atomic dynamics and different stationary states (e.g. lack of inflow of depolarized atoms), (v) ability to work with large optical densities (OD ~100 and more) without experiencing too strong decoherence, last-not-least (vi) possibility of exploring quantum-degeneracy regime, where ultra-low temperatures have, in fact, no alternative.

In this work, we describe preparation of rubidium atoms by laser cooling in a magneto-optical trap (MOT) and a set of diagnostic tools and protocols for precision control of magnetic fields, including non-stationary field monitoring that should prove helpful in many cold-atom experiments in the important temperature range 10–100 μK. In particular, they enable cold-atom vector magnetometry and characterization of tensorial, i.e. based on spatial symmetry, characterization of the atomic superpositions.

The created states are characterized by monitoring the polarization plane of light that passes through the medium. The effect of optical rotation in a magnetic field (Faraday effect) results from light detuning and population distribution[10–12]. Sufficiently strong light may not only probe, but also modify the atomic states and create their coherence[13–15] leading to the observation of the time-dependent, nonlinear magneto-optical rotation or nonlinear Faraday effect (NFE). This process is closely related with the electromagnetically induced transparency[16], electromagnetically induced absorption[17,18], coherent population trapping[19] and other manifestations of the interference effects in coherently prepared media[20,21].

Theoretical background

To relate atomic superposition states with experimentally measured observables we start with a standard relation between the complex refraction index and density matrix (see for example ref.[22])

M. Smoluchowski Institute of Physics, Jagiellonian University, Prof. Łojasiewicza 11, 30-348, Kraków, Poland. Correspondence and requests for materials should be addressed to K.S. (email: krystian.sycz@gmail.com)
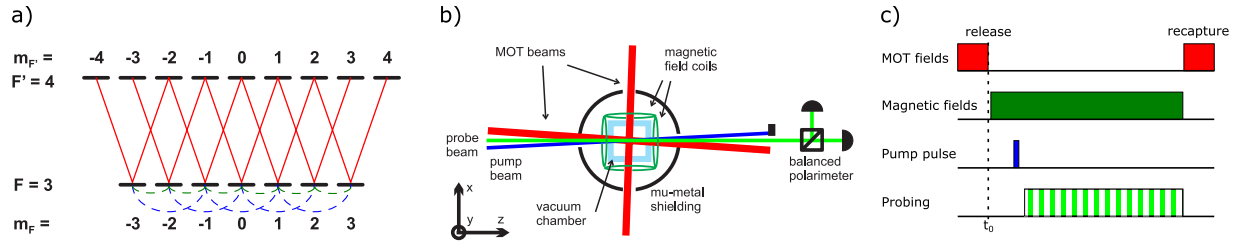
Figure 1. Schematics of the experimental arrangement. (**a**) A diagram of relevant Zeeman levels of ^{85}Rb, showing optical transitions caused by the linearly polarized light (red lines) and the $|\Delta m| = 2$ coherences it creates (dashed blue). Green dotted lines indicate $|\Delta m| = 1$ coherences created by the RF or static perpendicular field. (**b**) Schematic diagram of the experimental setup. (**c**) Timing sequence of the applied fields.

$$n_{\pm} - 1 \propto \mathcal{E}^{-1} \sum_{e,g} \mathcal{R}e\left(d_{eg}^{(\pm)} \rho_{eg}^{(\pm)}\right), \tag{1}$$

where ε is the light electric field amplitude, $d_{eg}^{(\pm)}$ are the matrix elements of the dipole moment associated with the $\sigma^{\pm}$-polarized light-beam components linking the ground (g) and excited (e) states, and $\rho_{eg}^{(\pm)}$ are the related density matrix elements. We consider an atomic system with magnetic degeneracy, i.e. with sublevels m and m' in states g and e of angular momenta F and F', respectively, and assume their linear Zeeman splitting (Fig. 1a).

The quantity directly measured in the experiment is the Faraday angle θ, which determines rotation of the polarization plane of a linearly polarized light beam that propagates through the atomic medium immersed in a magnetic field.

$$\theta \propto \mathcal{E}^{-1} \sum_{e,g} \mathcal{R}e\left(\rho_{eg}^{(+)} - \rho_{eg}^{(-)}\right). \tag{2}$$

The dependence of optical coherence $\rho_{eg}^{(\pm)}$ on laser frequency is responsible for the spectral dependence of the complex refractive index, which in the case when e, g are magnetic sublevels is also influenced by the magnetic field. The latter affects also Zeeman coherences $\rho_{ee'}$ and $\rho_{gg'}$. Consequently, in addition to the resonant factor prior to the summation sign in Eq. (2), optical coherences exhibit also Hanle-like resonances of Zeeman coherences around $B = 0$[23]. These resonances have characteristic widths which reflect relaxation rates $\gamma_m(\gamma_{m'})$ of states m (m')[24–26].

For a simple system with $F = 1$ and $F' = 0$ interacting with a longitudinal magnetic field along the quantization axis 0z the relevant sublevels of the ground state g are $|F = 1, m = \pm 1\rangle$ and for a small Zeeman splitting ($\omega_L \ll \Gamma$, Γ being the natural width of the transition) the rotation angle θ can be expressed as

$$\theta \propto \frac{\omega_L \left[\rho_{--} + \rho_{++} + 2Re(\rho_{-+})\right] + \delta(\rho_{--} - \rho_{++})}{\delta^2 + (\Gamma/2)^2}, \tag{3}$$

where $\omega_L = g_F \mu_B B$ denotes the Larmor frequency and δ is the probe-light detuning from the $F = 1 \leftrightarrow F' = 0$ resonance frequency (g_F is the Landé factor and μ_B the Bohr magneton). In the absence of coherence ρ_{-+}, the first term in Eq. (3) is responsible for the *diamagnetic* Faraday rotation. When population imbalance between the $|-\rangle$ and $|+\rangle$ sublevels is created, the second term in Eq. (3) reflects the, so called, *paramagnetic* rotation which occurs even without external magnetic field[27]. The two kinds of rotation exhibit different symmetries as a function of the light frequency and magnetic field: the *diamagnetic* contribution is characterized by symmetric Lorentzian line-shape as a function of δ, while the paramagnetic one has a dispersive shape which cancels when $\delta = 0$ (as a function of ω_L, the paramagnetic rotation is an even function, while the diamagnetic rotation is an odd function).

Optical pumping with circularly polarized light results in a spin *polarization* (non-zero magnetization), described by different populations of individual m magnetic sublevels, i.e. diagonal elements of the density matrix. On the other hand, linearly-polarized light may create *alignment* with no net spin polarization but a specific symmetry in populations of the $\pm m$ sublevels and a certain phase relation between them, i.e., the *coherence*, represented by the non-diagonal elements of density matrix. Due to the symmetry, linearly polarized light couples magnetic states with $|\Delta m| = 2$ (Fig. 1a) and greater even numbers for high-intensity (multiphoton) processes[28].

Evolution of atomic observables results from competition between the excitation, decay (relaxation and escape), coherent evolution stochastic noise and various instabilities. Its analysis may be simplified by using a short excitation pulse and interrogation by a weak probe. The short pulse creates elements of the density matrix responsible for state populations and coherences. The relaxation of the excited-stated quantities, governed by spontaneous emission, is usually much faster that the relaxation of the ground-state density matrix elements. Consequently, the elements associated with the excited state decay rapidly to zero, while those associated with the ground-state live much longer. After termination of the pump pulse at t_0, the elements associated with Zeeman sublevels undergo the free induction decay (FID) and exhibit the following time dependence

$$\rho_{gg'}(t) = \rho_{gg'}^{(0)} e^{-\gamma_{gg'}(t-t_0)} e^{-i\omega_{gg'}t}, \tag{4}$$

where $\rho_{gg'}^{(0)}$ is the amplitude of the ground-state density matrix element prepared by the pump pulse at t_0 and decaying with rate $\gamma_{gg'}$, and $\omega_{gg'} = \left(E_g - E_{g'}\right)/\hbar$ is the energy difference between states g and g' expressed in frequency units, i.e. the precession frequency of the coherence $\rho_{gg'}$:

$$\omega_{gg'} = |m - m'|\omega_{\mathrm{L}}, \tag{5}$$

where m, m' are the magnetic quantum numbers of the relevant atomic state.

In our experiments, we fix the quantization axis along the probe beam (0z) and focus on two situations: (*i*) precession of an atomic alignment (Zeeman coherences $\rho_{mm'}$ with $|\Delta m| = 2$ created by a linearly polarized light) around the longitudinal magnetic field, B_z, with frequency $2\omega_L$ and (*ii*) precession of an atomic polarization (coherences with $|\Delta m| = 1$ created by a circularly polarized light) around the transverse magnetic field $B_\perp \equiv \sqrt{B_x^2 + B_y^2}$ with frequency ω_L. The latter is associated with magnetic mixing of m sublevels differing by $|\Delta m| = 1$ by transverse fields. Consequently, time evolution of the ground-state coherences may exhibit two characteristic frequencies $2\omega_L$ and ω_L corresponding to polarization and alignment driven by B_z and $B_\perp$, respectively.

In the case of cold-atom experiments, the main relaxation mechanisms include atomic-state losses due to escape of atoms from the observation volume caused by ballistic expansion, optical pumping to non-interacting states or pushing atoms out of the trap, trap imperfections, and/or collisions with rest-gases, as well as dephasing due to magnetic field and light-shift (AC Stark effect) inhomogeneities.

Methods

The experiments were conducted using cold rubidium atoms (both [87]Rb and [85]Rb, consult Table 1 in Suppl. Info. for figure reference) released from a MOT. Experimental setup and timing sequence diagram are shown schematically in Fig. 1b,c, respectively. Cold rubidium samples are periodically released from the trap. After the MOT fields shut off, a specific spin distribution in the ground state is prepared using a short circularly- or linearly-polarized pump pulse, resonant with the trapping transition. Atoms then undergo precession in the applied magnetic field, while their interaction with stray fields is minimized by magnetic shielding of the trap. Independent beam with a variable detuning probes the birefringence of the expanding atomic cloud. The rotation of probe-beam polarization plane is recorded using precision balanced polarimeter and fast photodetectors. Finally, the trap is switched back on and the cycle is repeated.

Measured birefringence provides information on the ground state polarization and coherence and their evolution in the magnetic field. In a single beam experiment, the pumping pulse is omitted, and signals arising solely due to the interaction with a probe beam are recorded. Some experiments were performed with delayed or strobed probing to minimize the effects of light on the state evolution. More detailed description of experimental setup and procedures is enclosed in the Supplemental Information. Datasets acquired in this study are available from the corresponding author on reasonable request.

Results

Single-beam magneto-optical rotation. With a single linearly polarized beam two types of rotation resonances occurring around the zero-field value can be observed, shown in Fig. 2 as a function of the magnetic field B_z. A broad (several Gauss wide) resonance (Fig. 2a) results from a linear Faraday rotation, while the central, much narrower resonance (Fig. 2b) reflects the NFE caused by the Zeeman coherence[13,14]. Figure 2c shows the observed signals measured for different interaction times of atoms with light. The inset shows the expanded region of $B_z \approx 0$, with the distinct contribution of NFE caused by Zeeman coherence. While the broad (about 6 G wide), linear (with respect to the light intensity) rotation signal appears instantaneously after the measurement begins (blue curve), the narrow NFE resonance takes some build up time that depends on the beam intensity. The NFE resonance shown in Fig. 2b has a FWHM of 6.5 mG, which corresponds to a coherence lifetime of $\sim$100 μs. Figure 2d shows the rotation angle as a function of time for three values of B_z. The top curve ($B_z = 8$ mG) illustrates the buildup of the nonlinear effect on a short time-scale of about 2 ms, which is then limited by the atom-number losses caused by the light (heating and the related loss of coherence), freefall and ballistic expansion. The middle ($B_z = 2.2$ G) and the lowest ($B_z = 5.4$ G) curves show the immediate onset of the linear effect and its domination at short times. At longer times ($\sim$1 ms) the signals reflect changes of the population distribution caused by optical pumping, seen as inversion of the rotation sign of the middle trace. Eventually, for times $\gtrsim$5 ms the rotation signals tend to zero.

The narrow central part of the rotation curve that corresponds to the NFE rotation (Fig. 2b and inset to Fig. 2c) enables characterization of the Zeeman coherence of trapped atoms[13] and precise measurements of weak magnetic fields[13,15]. In particular, for fields where the Zeeman splitting is smaller than the relaxation rate γ of the atomic coherence, $g_F \mu_B B < \gamma$, the linear dependence $\theta(B_z) \propto B_z$ enables direct measurement of the field intensity if proper calibration is performed. Sensitivity of such measurement improves with increasing amplitude and decreasing width of the NFE resonance. In the case of cold atoms, the signal amplitude and hence the sensitivity changes over time. This differs from the case of hot atomic vapours, where stationary rotation can be observed as a result of atoms flying in and out of laser beam. The maximum rotation amplitude observed in a single beam experiment was of the order of $\sim$200 mrad for intensities above 10 μW/mm^2, at the cost of significant power broadening of the resonances.

The width of the NFE resonance corresponds to the effective decoherence rate γ, which results from various contributions. The most dominant are: light-induced losses γ_{light}, which depend on the light intensity (scattering
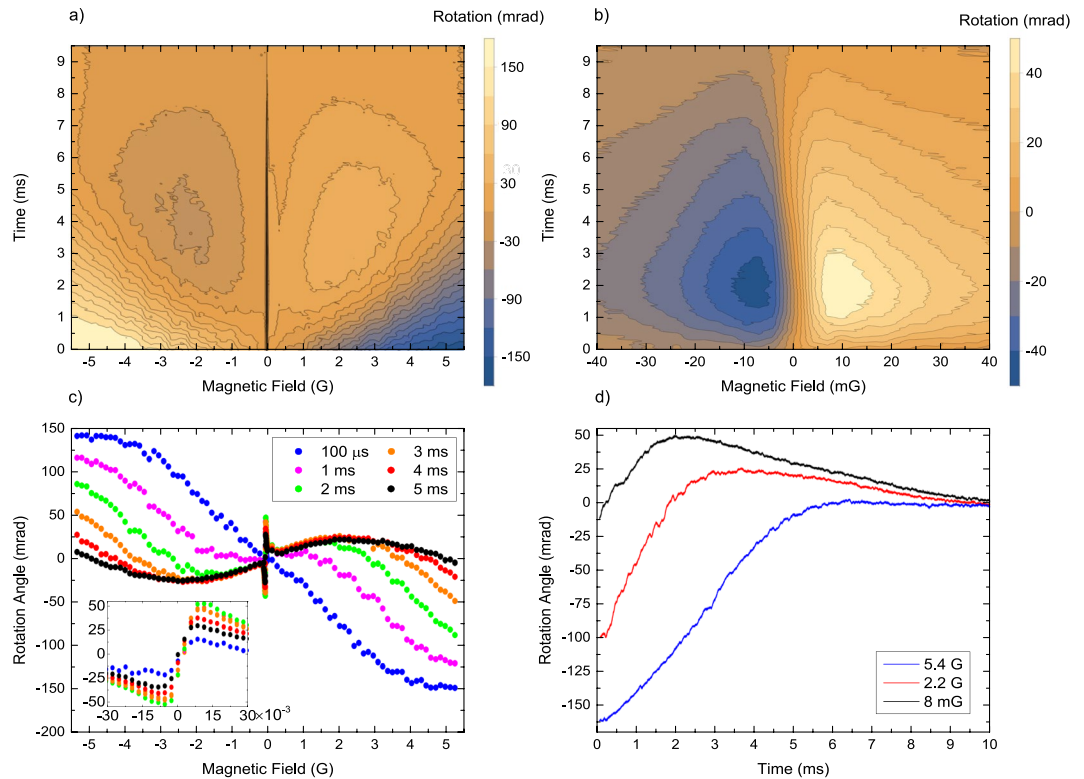
Figure 2. Faraday rotation observed with a single beam of 2.5 μW/mm² intensity, tuned to resonance. (**a**) Contour plot of the rotation angle dependence on magnetic field and time after switching on the light. (**b**) Expanded narrow central region of $B_z \approx 0$. (**c**) Horizontal cuts from (**a**) showing the rotation signals after 1, 2, 3, 4, 5 and 6 ms (top to bottom traces on the left side, respectively. (**d**) Time evolution of the rotation signal $\theta(B_Z)$ for magnetic-field values of: 8 mG (top black), 2 G (middle red), and 5.5 G (lowest blue).

rate), the atom-loss rate γ_{TOF} due to freefall and ballistic expansion of escaping atoms, and magnetic-field related decoherence γ_B due to uncompensated transverse fields, longitudinal field gradient as well as the oscillating fields and the field noise. The recorded resonance width reveals an effective decoherence rate $\gamma = \gamma_{TOF} + \gamma_{light} + \gamma_B$. When some of its constituents differ strongly, it may be possible to identify the dominating decoherence process and minimize it iteratively to optimize the net coherence lifetime.

Pump-probe measurements. Compared to the single-beam experiments, the use of separate beams for creation and probing of atomic states offers additional flexibility of pump polarization, detuning and intensity. Most importantly, however, it offers longer lifetimes of atomic polarization and coherence. In two-beam experiments a short pumping pulse creates a specific population distribution in the cold-atom sample and probe light is then used to record the time-dependent rotation. To minimize the probe's influence on atoms, it can be either attenuated, detuned from the optical resonance, and/or used in a strobed manner (see Supplemental Information). Signals associated with atomic polarization could be probed for a wide range of probe-beam detunings (up to several GHz). Already at 70 MHz detuning to the blue, and ~1 μW of light power rotation signals can be continuously probed for 15 ms without a discernible effect on the decay time. On the other hand, detection of atomic coherence is sensitive to the probe frequency, i.e. the rotation amplitude falls rapidly when the detuning increases above the natural width (Eq. (3)).

FID of atomic polarization. Optical pumping by circularly polarized pump pulses propagating along the 0z direction, creates a population imbalance between sublevels m and $-m$ that is equivalent to the sample's magnetization, or polarization along the pump beam, $\langle F_z \rangle \neq 0$, described by diagonal elements of density matrix.

Arbitrarily oriented DC magnetic field affects the atomic polarization induced by circularly polarized pump pulses in two ways: (*i*) When $\mathbf{B} \nparallel 0z$, the transverse components of the magnetic field mix the adjacent ($|\Delta m| = 1$) sublevels. The created atomic polarization undergoes Larmor precession with frequency $\omega_L = g_F \mu_B B$ proportional to the total field strength $B = \sqrt{B_x^2 + B_y^2 + B_z^2}$, with amplitude dependent on the direction of the field[29]. The sign of the rotation depends on the pump beam helicity (left- or right-handed) and on the sign of the probe beam detuning (Fig. 3b). (*ii*) For $B_x = B_y = 0$ and $B_z \neq 0$, there is no oscillation – the magnetization is stationary, and its decay is caused primarily by the decreasing number of atoms.

Figure 3a depicts precession of the atomic polarization observed after applying a relatively strong (~1 mW/mm²) and short (<20 μs) pump pulse, while switching on the homogenous magnetic field $B_x = 56$ mG, along
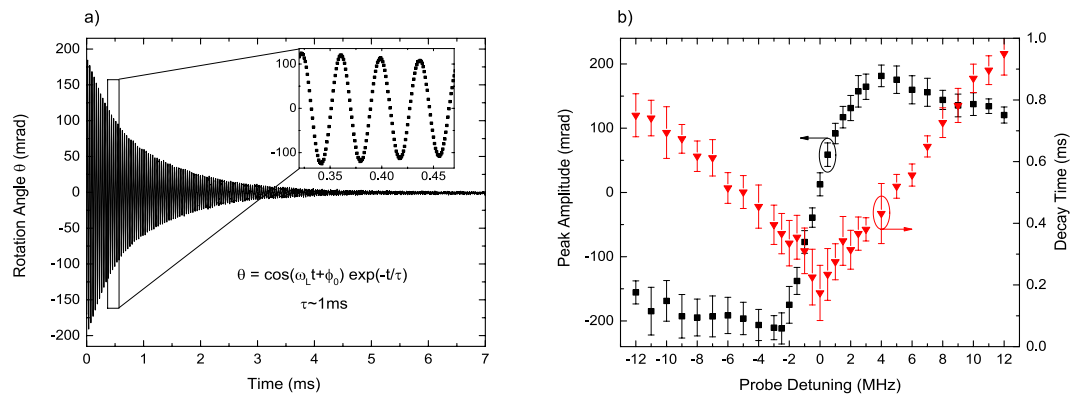
Figure 3. FID of atomic polarization. (**a**) Example signal for $B_x = 56$ mG, with the probe 70 MHz blue detuned from the atomic transition. (**b**) Amplitude (red triangles, left scale) and decay time (black squares and right scale) of the fitted FID signals near the atomic resonance vs the probe detuning δ. Data points are the mean values of 5 non-consecutive measurement series while the error bars show the standard deviation and are indicative of variations in the trapped atom number.

the 0_x direction at $t = 0$. The resulting rotation signal represents FID of atomic polarization, which oscillates at the Larmor frequency ω_L, which is the measure of the intensity of total magnetic field, while its decreasing amplitude reflects polarization relaxation and the decay of the number of interrogated atoms. Figure 3b illustrates the dependence of the amplitudes and decay times of the polarization FID signals on the probe detuning. Typically for paramagnetic rotation, the FID amplitude has a dispersive dependence on δ with a width close to $\Gamma/2\pi = 6$ MHz and vanishes at $\delta = 0$. Its decay exhibits strong decoherence by the resonant probe beam.

FID signals can be a useful indicator of the magnetic field alignment, homogeneity, and/or presence of parasitic stray fields. In the ideal case of magnetic field perfectly aligned along 0_x, the FID signal is symmetric around zero value with exponentially decaying envelope. Stray fields, gradients and instabilities cause non-exponential decay, asymmetry and variations in the oscillation frequency (Suppl. Info.).

FID of atomic coherences. Setting the pump beam polarization to linear enables the creation of Zeeman superpositions. Here, we focus on the coherences of Zeeman sublevels described by non-diagonal elements of density matrix with $|\Delta m| = 2$. The coherences contribute to atomic alignment and can be monitored by a linearly polarized probe beam as a rotation of its polarization plane[13–15]. In time-dependent measurements atomic alignment manifests as oscillations at the frequency of $2\omega_L$ and are usually damped faster than polarization signals (Fig. 4a,b).

While the creation and observation of Zeeman coherences under CW conditions is relatively straightforward and can be easily monitored as narrow NFE signals around $B_z \approx 0$ (Fig. 2), observations of these coherences at $B_z \neq 0$, and particularly their FID signatures, is by far more demanding. Transverse magnetic fields have to be carefully compensated and possibly the whole system shielded from any AC fields. The amplitude of the coherence signal rapidly decreases with the probe-beam detuning δ (black squares in Fig. 4c), thus, δ should be small, on the order of Γ. Unfortunately, small δ enhances decoherence of the alignment (red triangles in Fig. 4c). It is therefore optimal to pump with the resonant beam, and trade-off the intensity and detuning of the probe. Figure 4c depicts Lorentzian symmetry of the observed coherence FID signals, characteristic for diamagnetic rotation. It is usually beneficial to adjust the pump-pulse duration to the value of Larmor frequency. We observed that the decay rates of the atomic polarization and coherence differ strongly as shown in Fig. 4d for both signals recorded under identical probing conditions. The coherence decay time is consistently faster than for the polarization FID, and both increase at different rates with probe intensity. The slowest observable decay of coherence corresponded to approximately 0.5 ms. Observation of longer coherence lifetimes requires further probe beam attenuation, and may become impractical due to degradation of the signal-to-noise ratio. For this reason, we have employed the stroboscopic technique of relaxation in the dark discussed in Supplementary Information.

Zeeman superpositions in tilted magnetic field. When the magnetic field is tilted with respect to the probe field direction $0z$ the evolution of the Zeeman superpositions becomes more complicated. As described in ref.[30], when the magnetic field vector is tilted away from the $0z$ direction, in the plane of pump light polarization and propagation direction (YZ, angle α), the rotation becomes a superposition of two damped sine functions, one oscillating at $2\omega_L$ and the other at ω_L. Figure 5a depicts the rotation signal recorded in such a tilted magnetic field. In addition to the $|\Delta m| = 2$ coherence signal that oscillates at $2\omega_L$, a component oscillating at ω_L is also visible and can be interpreted as a manifestation of superpositions with $|\Delta m| = 1$. Since both components originate from the same atomic population distribution, they decay at the same rate. The amplitude of the $2\omega_L$ contribution diminishes with the tilt angle α, while the other one increases. From $\alpha = 45$ deg the contribution at ω_L becomes dominant. The pump-probe setup allows us to observe the described evolution in real time, and the analysis of such signals can be used to determine the tilt angle (black squares in Fig. 5b). Tilting the field in the direction perpendicular to both, the pump light polarization and propagation direction (XZ, angle β), does not introduce the modulation at ω_L, but reduces the oscillation amplitude (red triangles in Fig. 5b). With appropriate calibration, it
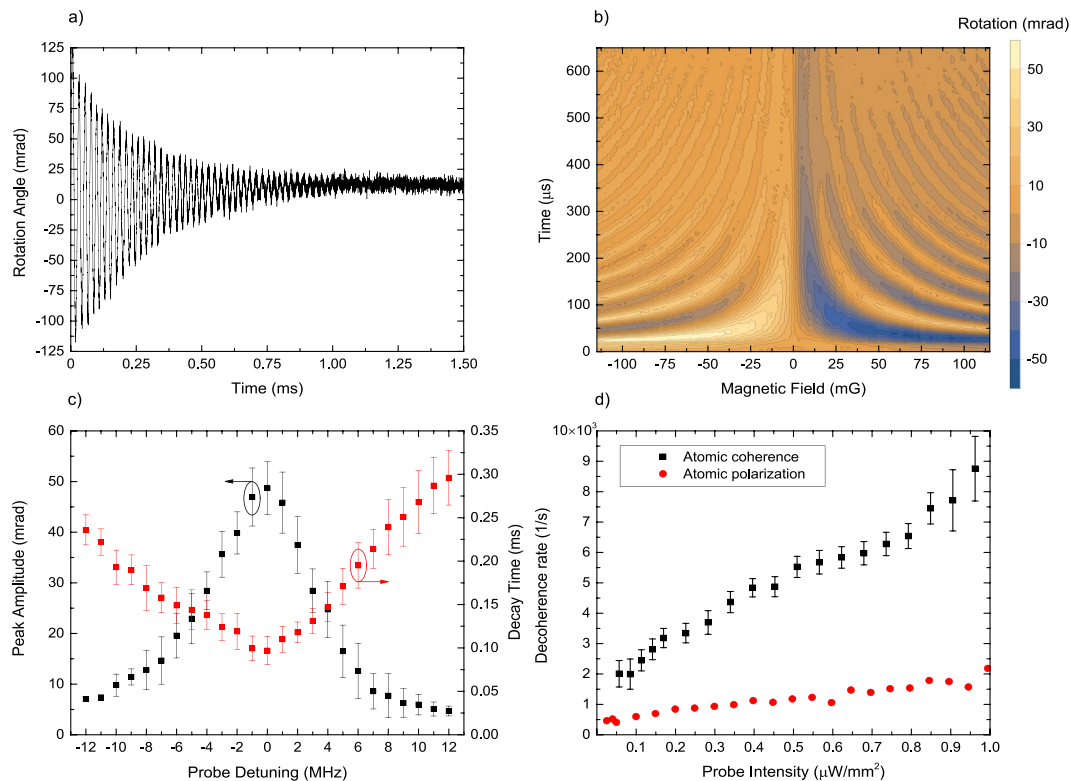
Figure 4. FID signal of atomic $|\Delta m| = 2$ coherence created by a linearly-polarized pump pulse propagating along the probe beam: (**a**) time dependence of the rotation signal $\theta(t)$ in magnetic field $B_z = 95$ mG, under continuous probing. (**b**) FID signal of atomic coherence $\theta(B_z, t)$ as a function of time and B_z. (**c**) The amplitude and decay time of the coherence FID signals dependence on the probe detuning. (**d**) Decay rates of atomic polarization and coherence on the probe light intensity (CW probing with light detuned by 24 MHz to the blue). Error bars like in Fig. 3.
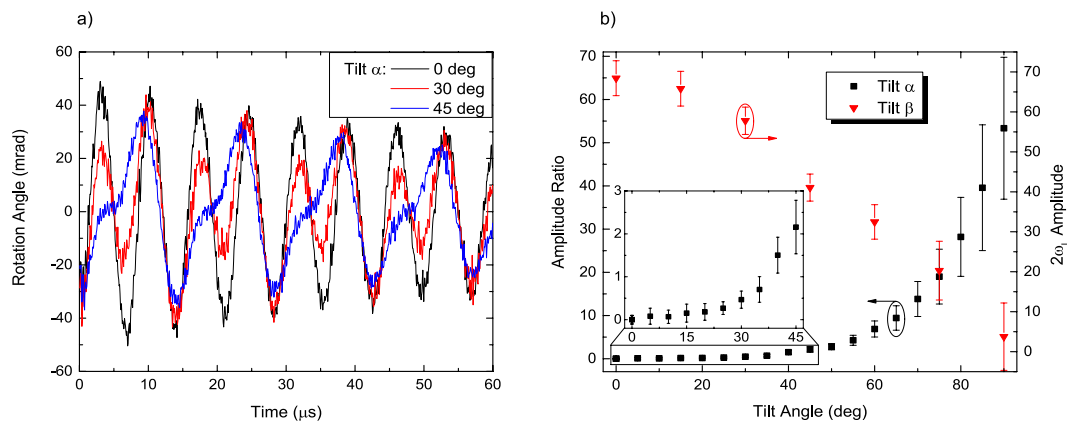
Figure 5. Coherence FID signals in tilted fields (with pump light polarized in the $0y$ direction). (**a**) Modification of the signals as the field is tilted away from the $0z$ direction and towards $0y$ by an angle α. A bimodal character is clearly visible. (**b**) The ratio of the amplitudes of components $A(\omega_L)/A(2\omega_L)$ changes as $\tan\alpha$ and can be used to determine the tilt angle (black squares). The inset shows the zoomed in low tilt angle region. Tilting of the field towards the $0x$ direction results only in diminishing amplitude of the oscillations $A(2\omega_L)$ as the $\cos\beta$ (red triangles). Error bars like in Fig. 3.

is possible to exploit this effect for vector magnetometry. Similar results have been discussed by the Weis and Riis groups[31,32], while an alternative method of vector magnetometry has been proposed in refs[33,34].

Detection of radio-frequency fields. An unequal distribution of atomic population among Zeeman sub-levels caused by optical pumping enables us to use the magnetic resonance technique, known as radio-optical
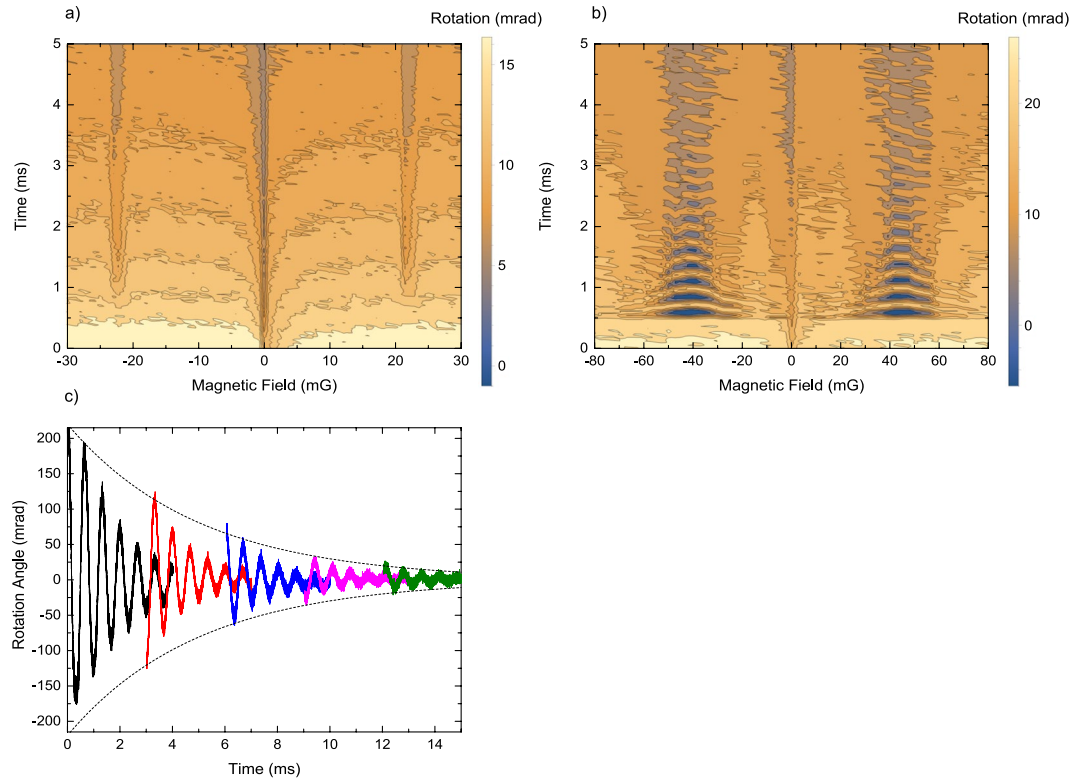
Figure 6. RF induced ODMR signals recorded as a function of B_z and time in two RF-intensity regimes: $\Omega_R \lessgtr \gamma_{gg'}$. (**a**) Weak-field regime, $B_{RF} \approx 200\,\mu G$ at $\omega_{RF} = 2\pi\,10\,kHz$. The dashed line indicates time at which RF field is turned on. (**b**) Strong-field regime, $B_{RF} \approx 7\,mG$ at $\omega_{RF} = 2\pi\,20\,kHz$, revealing RF induced Rabi oscillations seen as horizontal bell-shaped fringes. Minimum oscillation frequency is around $+/-43\,mG$. The central feature in both figures is an artefact of the sample preparation process. (**c**) A signal of RF induced Rabi oscillations observed by the relaxation in the dark method. The individual signals decay with $\tau = 1.56\,ms$, while the envelope with $\tau = 5\,ms$; a rate that is comparable with the calculated rate of atoms leaving the interaction area.

double resonance or optically detected magnetic resonance (ODMR). ODMR in a system of Zeeman sublevels is a popular method applied in many situations including cold-atom magnetometry[15]. Below, we present an application of the technique for detection of RF magnetic fields. A short circularly polarized pump pulse creates an atomic polarization along the probe beam (0z axis, as in the case of atomic polarization), while magnetic field B_z splits the sublevels by ω_L. A transverse RF field of frequency ω_{RF} matching the Zeeman splitting alters the population distribution which can be monitored via rotation of the probe beam polarization.

Depending on the Rabi frequency for the RF field-atom interaction, $\Omega_R = \mu_B B_{RF}$, where B_{RF} is the amplitude of the magnetic component of the RF field, two different regimes of the RF field interaction with atomic sample can be investigated: the weak- and the strong-field one. Figure 6b presents contour plots illustrating the ODMR rotation resonances for both regimes with RF frequency on the order of tens of kHz as a function of B_z and time. In the weak-field regime, where $\Omega_R < \gamma_{gg'}$, the ODMR signals manifest as vertical stripes occurring at two resonant frequencies, $\omega_{RF} = \omega_L$. By tuning ω_{RF} to the Zeeman splitting of $\pm\omega_L$ one can measure the magnetic field intensity.

In the strong field regime, $\Omega_R > \gamma_{gg'}$, the stripes as a function of time exhibit distinct structure of Rabi oscillations (Fig. 6b) with frequency

$$\Omega'_R = \sqrt{(\omega_{RF} - \omega_L)^2 + \Omega_R^2}. \tag{6}$$

Figure 6b reveals also teh characteristic bell-shape bending of the oscillation fringes around the resonance centre which is due to the difference between the resonant and non-resonant values Ω_R and Ω'_R. By measuring the Rabi frequency, we are able to measure the RF field intensity. Assuming that we need at least one period of Rabi oscillations to determine Ω_R, the decay time of the polarization sets the floor of $150\,\mu G$ on the measurable RF intensities in our current setup.

Like in the case of coherence FID signals damping rate of the observed Rabi oscillations is also affected by the probe-beam intensity. The relaxation in the dark method can be used to maximally extend the available observation time, as seen in Fig. 6c.

Discussion

We have presented a set of simple yet versatile diagnostics and optimization tools for experiments with cold atoms where well-controlled atomic superpositions could be produced and characterized. The fundamental limitation of the coherence lifetime of atoms released from a trap is their ballistic expansion and escape from the detection region. This may be substantially extended by using conservative traps which enable interaction with trapped atoms and offer trapping times on the order of minutes[35]. The described methods could then contribute to achieving very long coherence lifetime and, hence, much higher magnetometric sensitivity.

We have demonstrated that even on a 10 ms time scale of ballistic expansion from the MOT several decoherence processes which affect superposition states can be identified. For superposition of states with differing magnetic quantum numbers important decoherence mechanisms are the inhomogeneity and instability of the external magnetic field (see also Figs S2 and S4 in Suppl. Inform). These may be suppressed by a proper magnetic shielding and usage of stable current sources for field generation. Another major source of decoherence is the effect of the probe beam intensity, that can be reduced by detuning the light from resonance, at the expense of the amplitude of coherence signals. An alternative and practical solution is the strobing of the probe light to minimize the interaction time (see also S3 of Suppl. Info.) while maintaining low detuning and relatively high intensity.

The described experiments demonstrate that the coherence/superposition states of investigated cold-atom samples live shorter than the states characterized by atomic polarization (populations). Sensitivity of the former ones to light and magnetic field stability and uniformity requires the usage of magnetic shielding, mains synchronization, observations with strobe light or the relaxation in the dark method in order to observe a comparable lifetime.

We have also demonstrated *in situ* diagnostics of the magnetic fields in the cold atom sample region, using magneto- optical rotation caused by atomic polarization and superposition states. These methods can be used for a wide range of cold-atom experiments, like for precise monitoring of atomic states during quantum state manipulation experiments, calibration of magnetic field sources, compensation of external fields, or for laser detuning diagnostics.

References

1. Metcalf, H. J. & van der Straten, P. *Laser Cooling and Trapping* (Springer 1999).
2. Cronin, A. D., Schmiedmayer, J. & Pritchard, D. Atom Interferometers. *Rev. Mod. Phys.* **81**, 1051 (2009).
3. Ludlow, A. D., Boyd, M. M., Jun Ye., Peik, E. & Schmidt, P. O. Optical atomic clocks. *Rev. Mod. Phys.* **87**, 637–701 (2015).
4. Boyd, R. W. & Gauthier, D. J. "Slow" and "Fast" Light. Chapter 6 in *Progress in Optics*. **Vol. 43** (ed. Wolf, E.) 497–530 (Elsevier, Amsterdam, 2002).
5. Shore, B. W. Coherent Manipulations of Atoms Using Laser Light. *Acta Physica Slovaca* **58**, 243–486 (2008).
6. Shore, B. W. Pre-history of the Concepts Underlying Stimulated Raman Adiabatic Passage (STIRAP). *ibid.* **63**, 361–481 (2013).
7. Volz, J. *et al.* Observation of Entanglement of a Single Photon with a Trapped Atom. *Phys. Rev. Lett.* **96**, 30404 (2006).
8. Fano, U. Description of States in Quantum Mechanics by Density Matrix and Operator Technique. *Rev. Mod. Phys.* **29**, 74 (1957).
9. Cohen-Tannoudji, C., Dupont-Roc, J. & Grynberg, G. *Atom-Photon Interactions. Basic Processes and Applications* (Wiley 1998).
10. Franke-Arnold, S., Arndt, M. & Zeilinger, A. Magneto-optical effects with cold lithium atoms. *J. Phys. B* **34**, 2527–2536 (2001).
11. Labeyrie, G., Miniatura, C. & Kaiser, R. Large Faraday rotation of resonant light in a cold atomic cloud. *Phys. Rev. A* **64**, 033402 (2001).
12. Gajdacz, M. *et al.* Non-destructive Faraday imaging of dynamically controlled ultracold atoms. *Rev. Sci. Instr.* **84**, 083105 (2013).
13. Wojciechowski, A., Corsini, E., Zachorowski, J. & Gawlik, W. Nonlinear Faraday rotation and detection of superposition states in cold atoms. *Phys. Rev. A* **81**, 053420 (2010).
14. Sycz, K., Wojciechowski, A. M. & Gawlik, W. Magneto-optical effects and rf magnetic field detection in cold rubidium atoms. *J. Phys. Conf. Series* **497**, 0120062014 (2014).
15. Gawlik, W. & Higbie, J. Magnetometery with cold atoms, Chapter 9 in *Optical Magnetometry* (eds Budker, D. & Jackson Kimball, D. F.) 167–189 (Cambridge Univ. Press, Cambridge, 2013).
16. Fleischhauer, M., Imamoglu, A. & Marangos, J. P. Electromagnetically induced transparency: Optics in coherent media. *Rev. Mod. Phys.* **77**, 633 (2005).
17. Akulshin, A. M., Barreiro, S. & Lezama, A. Electromagnetically induced absorption and transparency due to resonant two-field excitation of quasidegenerate levels in Rb vapor. *Phys. Rev. A* **57**, 2996–3002 (1998).
18. Lezama, A., Barreiro, S. & Akulshin, A. M. Electromagnetically induced absorption. *ibid.* **59**, 4732–4735 (1999).
19. Arimondo, E. Coherent population trapping in laser spectroscopy in *Progress in Optics* **35** (ed. Wolf, E.) 259–354 (Elsevier, Amsterdam, 1996).
20. Drampyan, R., Pustelny, S. & Gawlik, W. Electromagnetically Induced Transparency versus Nonlinear Faraday Effect. Coherent Control of the Light Beam Polarization. *Phys. Rev. A* **80**, 033815 (2009).
21. Witkowski, M. *et al.* Matter-wave interference versus spontaneous pattern formation in spinor Bose-Einstein condensates. *Phys. Rev. A* **88**, 025602 (2013).
22. Gawlik, W. & Pustelny, S. Nonlinear Faraday Effect and its Applications in *Horizons in World Physics: New trends in quantum coherence and nonlinear optics*. vol. **263** (ed. Drampyan, R.) 45–82 (Nova Science Publishers, New York, 2009).
23. *The Hanle Effect and Level-Crossing Spectroscopy* (eds Moruzzi, G. & Strumia, F.) 47–85 (Plenum Press, New York, London, 1991).
24. Budker, D. *et al.* Resonant nonlinear magneto-optical effects in atoms. *Rev. Mod. Phys.* **74**, 1153–1201 (2002).
25. Cohen-Tannoudji, C. *Atoms in strong resonant fields* in Frontiers in Laser Spectroscopy, Les Houches, Session XXVII (ed. Balian, R., Haroche, S., Liberman, S.) p. 1 (North-Holland, Amsterdam, 1977).
26. Decomps, B., Dumont, M. & Ducloy, M. *Laser Spectroscopy of Atoms and Molecules* in Topics in Applied Physics, Vol. 2 (ed. Walther, H.) p. 284 (Springer, Berlin, 1976).
27. Manuel, J. & Cohen-Tannoudji, C. Détection optique de la résonance magnétique par modulation de l'effet Faraday paramagnétique transversal à la fréquence de Larmor. *C. R. Acad. Sci.* **257**, 413 (1963).
28. Yashchuk, V. V. *et al.* Selective Addressing of High-Rank Atomic Polarization Moments. *Phys. Rev. Lett.* **90**, 253001 (2003).
29. Breschi, E. & Weis, A. Ground-state Hanle effect based on atomic alignment. *Phys. Rev. A* **86**, 053427 (2012).
30. Pustelny, S. *et al.* Nonlinear magneto-optical rotation with modulated light in tilted magnetic fields. *Phys. Rev. A* **74**, 063420 (2006).
31. Weis, A., Bison, G. & Pazgalev, A. S. Theory of double resonance magnetometers based on atomic alignment. *Phys. Rev. A* **74**, 033401 (2006).
32. Ingleby, S. J., O'Dwyer, C., Griffin, P. F., Arnold, A. S. & Riis, E. Orientational effects on the amplitude and phase of polarimetry signals in double-resonance atomic magnetometry. *Phys. Rev. A* **96**, 013429 (2017).
33. Behbood, N. *et al.* Real-time vector field tracking with a cold-atom magnetometer. *Appl. Phys. Lett.* **102**, 173504 (2013).

34. Smith, A., Anderson, B. E., Chaudhury, S. & Jessen, P. S. Three-axis measurement and cancellation of background magnetic fields to less than 50 μG in a cold atom experiment. *J. Phys. B: At. Mol. Opt. Phys.* **44**, 205002 (2011).
35. Gibbons, M. J., Kim, S. Y., Fortier, K. M., Ahmadi, P. & Chapman, M. S. Achieving very long lifetimes in optical lattices with pulsed cooling. *Phys. Rev. A* **78**, 43418 (2008).

Acknowledgements

Author Contributions

A.M.W. and W.G. conceived the study. K.S. performed experiments, and all authors analysed data, discussed the results and wrote the manuscript.

Additional Information

Supplementary information accompanies this paper at https://doi.org/10.1038/s41598-018-20522-x.

Competing Interests: The authors declare no competing interests.

Publisher's note: Springer Nature remains neutral with regard to jurisdictional claims in published maps and institutional affiliations.